Topological phase transition in the layered magnetic compound MnSb$_2$Te$_4$: Spin-orbit coupling and interlayer coupling dependence

Liqin Zhou [1,2] Zhiyun Tan,[1,3] Dayu Yan,[1,2] Zhong Fang,[1,2] Youguo Shi,[1,2,*] and Hongming Weng [1,2,4,†]

[1]*Beijing National Laboratory for Condensed Matter Physics and Institute of Physics, Chinese Academy of Sciences, Beijing 100190, China*
[2]*University of the Chinese Academy of Sciences, Beijing 100049, China*
[3]*School of Physics and Electronic Science, Zunyi Normal University, Zunyi 563006, Guizhou, China*
[4]*Songshan Lake Materials Laboratory, Dongguan, Guangdong 523808, China*

Based on the first-principles calculations and theoretical analysis, we investigate the electronic structures, topological phase transition (TPT), and topological properties of the layered magnetic compound MnSb$_2$Te$_4$. We have synthesized a MnSb$_2$Te$_4$ sample and determined its crystal structure. It has a crystal similar to that of the magnetic topological insulator MnBi$_2$Te$_4$ but has Mn and Sb site mixing. For the ideal case without such site mixing, our calculation indicates MnSb$_2$Te$_4$ is antiferromagnetic (AFM), and there is no band inversion at Γ. The band inversion can be realized by increasing the spin-orbit coupling (SOC) of Sb by more than 30%, and this results in a TPT from a trivial AFM insulator to an AFM topological insulator or an axion insulator. The compressive uniaxial strain can also drive a similar TPT if the interlayer distance is shortened by more than 5%. For the ferromagnetic (FM) case without Mn and Sb site mixing, it is a normal FM insulator. The band inversion can happen when SOC is enhanced by 10% or the interlayer distance is decreased by more than 1%. Thus, FM MnSb$_2$Te$_4$ can be tuned to be the simplest type-I Weyl semimetal with only one pair of Weyl nodes on the threefold rotational axis, which is different from the proposal that Mn and Sb site mixing can result in a ferrimagnetic state and a type-II Weyl semimetal state.

I. INTRODUCTION

Topological insulators (TIs) of Z_2 classification protected by time-reversal symmetry are characterized by the gapless topological boundary states with Dirac-cone-like dispersion. They have attracted intensive studies in the field of condensed-matter physics [1–4]. When magnetism is induced into TIs, the gapless topological boundary states are expected to be gapped, and various exotic topological phenomena will emerge, including the topological magnetoelectric effect [5,6], an axion insulator [7–11], and the quantum anomalous hall effect (QAHE) [12–16]. The typical three-dimensional (3D) TIs of the Bi$_2$Se$_3$ family have provided a fertile field to host many of these exotic phenomena [17,18], especially the QAHE in (Cr, V)-doped (Bi, Sb)$_2$Te$_3$ thin films [13,19,20]. Recently, the magnetic layered material MnBi$_2$Te$_4$ family was proposed theoretically to be a magnetic TI, which was confirmed by experimental studies immediately [21–35]. It crystalizes in a layered structure with the $R\bar{3}m$ space group (No. 166). Each layer is a septuple layer (SL) composed of Te-Bi-Te-Mn-Te-Bi-Te in a triangle lattice [36], and these SLs stack through van der Waals interaction. The magnetic ground state of MnBi$_2$Te$_4$ is a layered antiferromagnetic (AFM) state. In each SL, the magnetic moments of Mn ions point out of the plane, forming the ferromagnetic (FM) ordering, and they are

antiparallel to those in the neighboring SLs. When the number of SLs varies, the thin film of MnBi$_2$Te$_4$ can change from FM (a single SL) to compensated AFM (an even number of SLs) and uncompensated AFM (an odd number of SLs) [27]. Within the external field, it can also possibly be tuned to be FM. Therefore, experimental evidence of the Chern insulator, the axion insulator, AFM TIs, and a type-II Weyl semimetal (WSM) state has been realized [37] in the MnBi$_2$Te$_4$ system. The layered crystal structure, layered AFM configuration, and tunable magnetic orders with external magnetic field make it highly attractive in both fundamental research and potential applications.

MnBi$_2$Te$_4$ can be viewed as intercalating a Mn-Te bilayer into the center of a Bi$_2$Te$_3$ quintuple layer. There arises a question of whether the topological properties can be preserved when we replace the Bi$_2$Te$_3$ quintuple layer with Sb$_2$Te$_3$, which is also a 3D strong TI of the same family. However, the spin-orbit coupling (SOC) strength of Sb $5p$ orbitals (λ_{Sb} = 0.4 eV) is far less than that of Bi $6p$ orbitals (λ_{Bi} = 1.25 eV). We would like to study how the topological states of MnSb$_2$Te$_4$ are influenced by the SOC and even the interlayer interaction among SLs. In fact, Murakami *et al.* [30] recently proposed that it is possible to realize a FM or ferrimagnetic (FiM) state in MnSb$_2$Te$_4$ due to the site mixing of Mn and Sb atoms. They also proposed the FM state might be a type-II WSM based on their calculations. Furthermore, Shi *et al.* [38] observed an anomalous Hall effect in MnSb$_2$Te$_4$, supporting the FM or FiM order in MnSb$_2$Te$_4$. Here, we use the same flux method to synthesize single crystals of MnSb$_2$Te$_4$ and find the

*ygshi@iphy.ac.cn
†hmweng@iphy.ac.cn

TABLE I. Crystallographic data of $MnSb_2Te_4$.

Atom	x	y	z	Occupancy	Wyckoff position	Symmetry
Mn1	0.00000	1.00000	0.50000	0.680	3b	$-3m$
Sb1	0.00000	1.00000	0.50000	0.320	3b	$-3m$
Te1	0.33333	0.66667	0.45887	1	6c	$3m$
Mn2	0.66667	0.33333	0.40824	0.172	6c	$3m$
Sb2	0.66667	0.33333	0.40824	0.828	6c	$3m$
Te2	1.00000	0.00000	0.36864	1	6c	$3m$

mixing of Mn and Sb sites, too. In this work, we investigate the topological phase transition through the calculations of the ideal crystal structure to eliminate the complex sample-dependent site-mixing effect.

II. METHOD

To obtain the electronic structures of $MnSb_2Te_4$, we use the Vienna *Ab initio* Simulation Package (VASP) with the projector augmented-wave method based on the density functional theory (DFT) [39,40]. The Perdew-Burke-Ernzerhof (PBE) exchange-correlation functional with the generalized gradient approximation (GGA) $+ U$ method is used to treat the localized $3d$ orbitals of Mn [41–43]. The cutoff energy for the plane-wave basis is set at 520 eV, and the U parameter is selected to be 4 eV for Mn $3d$ orbitals. SOC is included self-consistently, and we set the local magnetic moment on Mn ions to be along the c axis. The Brillouin zone (BZ) integral is implemented on a Γ-centered grid mesh of $11 \times 11 \times 11$ for self-consistent calculations. The surface states and Fermi arc are calculated by using the WANNIERTOOLS software package based on the maximally localized Wannier functions [44,45].

Single crystals of $MnSb_2Te_4$ were synthesized by using the flux method. The starting materials Mn (piece, 99.99%), Sb (grain, 99.9999%), and Te (lump, 99.9999%) were mixed in an Ar-filled glove box at a molar radio of Mn:Sb:Te = 1:10:16. The mixture was placed in an alumina crucible, which was then sealed in an evacuated quartz tube. The tube was heated to 700 °C over 10 h and kept at that temperature for 20 h. Then, the tube was slowly cooled down to 630 °C at a rate of 0.5 °C/h followed by separating the crystals from the flux by centrifuging. Shiny crystals with a large size were obtained on the bottom of the crucible.

To investigate the crystalline structure, single-crystal x-ray diffraction (XRD) was carried out on a Bruker D8 Venture diffractometer at 293 K using Mo $K\alpha$ radiation ($\lambda = 0.71073$ Å). The crystalline structure was refined with the full-matrix least-squares method on F^2, where F is the structure factor describing how a material scatters incident radiation and the squared modulus F^2 gives the scattering intensity, using SHELXL-2016/6 program. The detailed crystallographic parameters are summarized in Table I. The single-crystal XRD study revealed that $MnSb_2Te_4$ has the same structure as $MnBi_2Te_4$. The lattice parameters of $MnSb_2Te_4$ are $a = 4.2613$ Å and $c = 41.062$ Å. Figure 1(a) shows the XRD patterns of a flat surface of a $MnSb_2Te_4$ single crystal, where only 00l peaks are detected. A photograph of a typical $MnSb_2Te_4$ crystal is shown in the inset of Fig. 1(b), and the 1-mm back bar indicates the size of

the crystal. Although there is mixing of Mn and Sb sites that might cause the FM state in $MnSb_2Te_4$, we take the ideal crystal structure without such mixing in the calculations. A schematic drawing of the ideal crystal structure based on the experimental one is shown in Fig. 1(c). In space group number 166, symmetric operations mainly include threefold rotation symmetry around the z axis C_{3z}, twofold rotation symmetry around the x and y axes, and inversion symmetry.

III. RESULTS AND DISCUSSION

A. AFM state of $MnSb_2Te_4$

Similar to $MnBi_2Te_4$, the layered AFM state of $MnSb_2Te_4$ has six formula units in a conventional unit cell, whose rhombohedral primitive cell is shown in Fig. 2(a). The AFM state has a combined symmetrical operation $S \equiv \Theta\tau_{1/2}$, namely, the time-reversal operator Θ and the translation operator of the half unit cell $\tau_{1/2}$ of the AFM lattice. $\tau_{1/2}$ is formed by the nearest neighbor's opposite spin moment of Mn atom layers. According to the GGA $+ U$ calculation, we find that the total energy of the AFM state is lower than that of the FM state by about 1.39 meV per formula unit when SOC is considered. The band structures of $MnSb_2Te_4$ for the AFM state without and with SOC are shown in Figs. 2(c) and 2(d), respectively. There is a direct gap of about 0.28 eV at the Γ point without SOC, which reduces to about 0.075 eV when SOC is considered. Although the magnetism breaks the time-reversal symmetry, the spatial inversion symmetry I and the combined symmetry S are preserved [21,22,46]. Therefore, the topological invariant Z_2 protected by S can be obtained through the parity eigenvalue or the evolution of hybrid Wannier charge centers (WCCs) of occupied states to judge the topological properties of the AFM state [2,47,48]. The parities of occupied states at the Γ point and three equivalent F points $(\pi, \pi, 0)$ indicate that $MnSb_2Te_4$ is not an AFM TI protected by S, which is consistent with the absence of band inversion at Γ. Since $MnBi_2Te_4$ is an AFM TI and the SOC strength of Sb $5p$ orbitals is obviously smaller than that of Bi $6p$, we manipulate λ_{Sb} artificially to demonstrate that topological phase transition can be caused by increasing SOC.

The SOC strength of Sb p orbitals, which is parameterized as λ_{Sb}, should be tuned in the self-consistent calculations [31]. The band structures for the AFM phase with 1.3 and 1.5 times the initial SOC strength λ_0 are shown in Figs. 3(a) and 3(b), respectively. Obviously, when $\lambda_{Sb} = 1.3\lambda_0$, the band gap at Γ closes, while when $\lambda_{Sb} = 1.5\lambda_0$, the gap reopens. We find
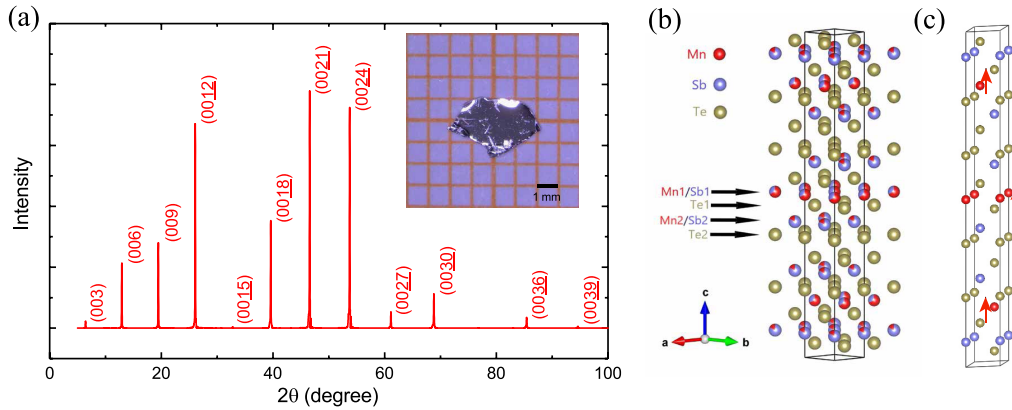
FIG. 1. (a) The x-ray diffraction pattern of a flat surface of a $MnSb_2Te_4$ single crystal. The inset shows a photograph of a typical $MnSb_2Te_4$ single crystal. (b) The schematic crystalline structure of $MnSb_2Te_4$ from experiment with Mn and Sb site mixing. (c) The schematic drawing of the ideal crystal structure for $MnSb_2Te_4$ without mixing of Mn and Sb sites. The arrows around Mn indicate the local magnetic moment on it.

that $MnSb_2Te_4$ changes from an AFM normal insulator to an AFM TI, which means that band inversion has occurred by increasing SOC and $1.3\lambda_0$ is the critical point of the topological phase transition. According to the critical value of SOC, it is possible to make a series of samples of $MnSb_xBi_{2-x}Te_4$ to study the topological phase transition.
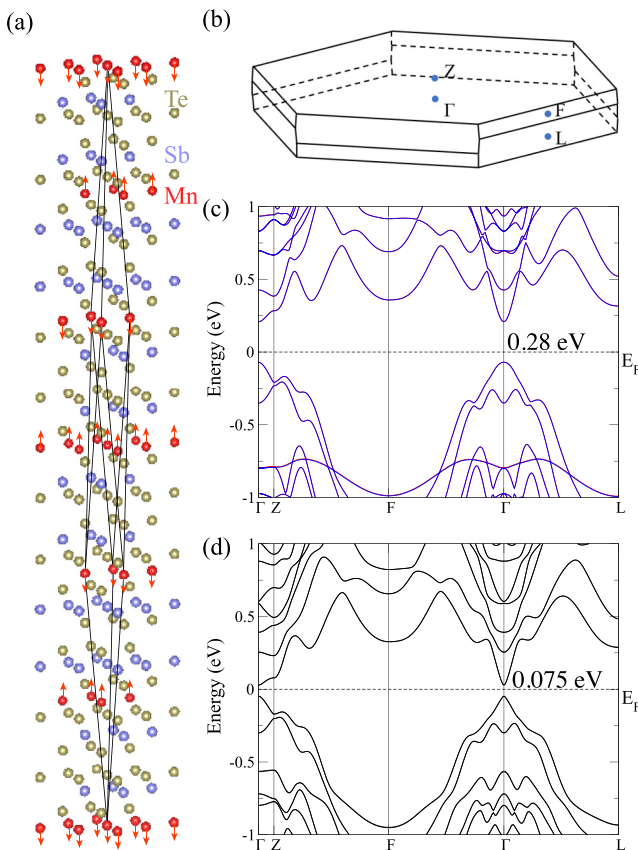

FIG. 2. Crystal structure and electronic structure of AFM $MnSb_2Te_4$. (a) The primitive cell of AFM $MnSb_2Te_4$; the red arrows represent the spin moment of the Mn atom. (b) The first Brillouin zone and four inequivalent TRIM points of $MnSb_2Te_4$. The band structure of AFM state (c) without and (d) with SOC.
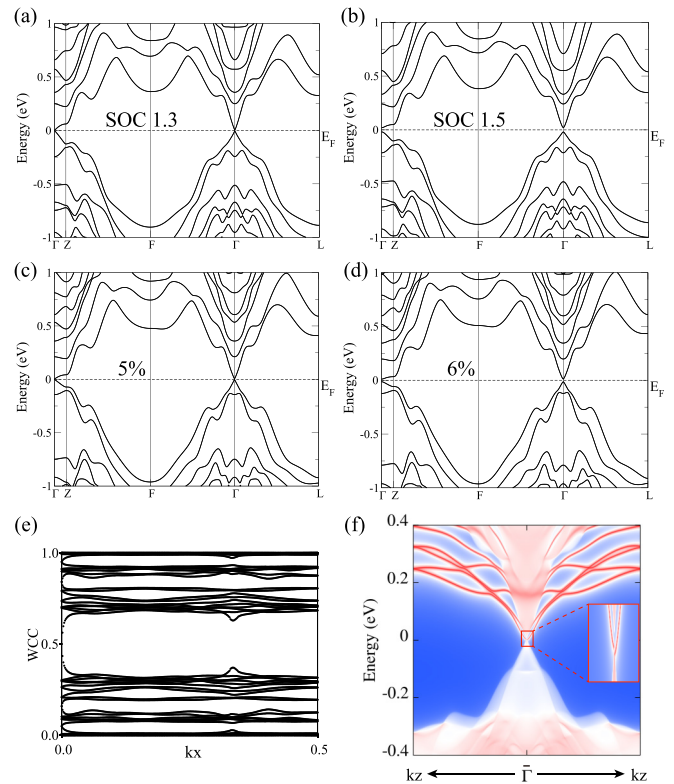

FIG. 3. The electronic structures of AFM $MnSb_2Te_4$ under different conditions. (a) and (b) Band structures for SOC strength λ_{Sb} of Sb change to 1.3 times and 1.5 times the initial value, respectively. (c) and (d) The band structure with the interlayer distance decreased by 5% and 6% along the z axis with SOC, respectively. (e) Evolution of WCCs in the $k_z = 0$ plane of AFM $MnSb_2Te_4$ under 6% compressive strain. This implies a nonzero topological invariant. (f) The surface states on the $(1\bar{1}0)$ surface. The Dirac-cone-like surface bands are magnified around $\bar{\Gamma}$.
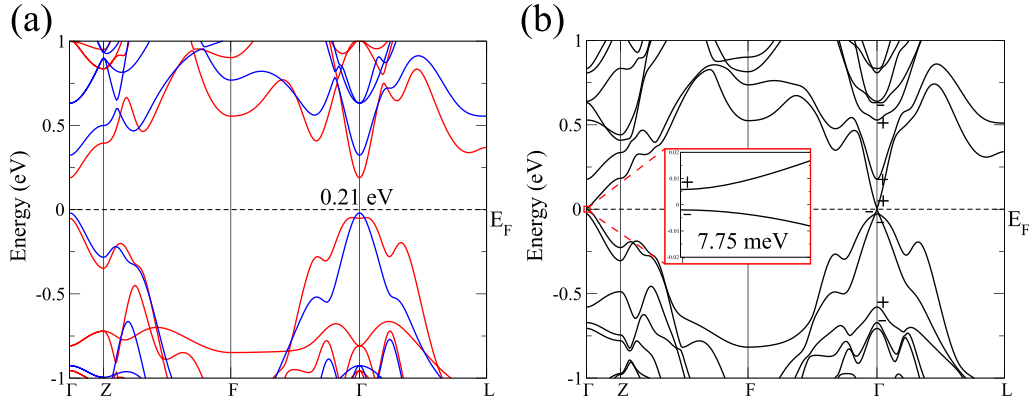
FIG. 4. The electronic structures of FM MnSb$_2$Te$_4$. (a) and (b) The band structures of the FM state (a) without and (b) with SOC [red bands indicate spin up, and blue bands indicate spin down in (a)].

In addition to directly adjusting the SOC strength λ_{Sb} in an experimental sample synthesized through alloying Sb and Bi, we try to simulate the topological phase transition by applying pressure or strain to MnSb$_2$Te$_4$. This is another usual way to control the physical properties of solids. We simulate the uniaxial compressive strain along the z axis by decreasing the interlayer distance among septuple layers along the c lattice vector. The band structures with c decreased by 5% to 6% are shown in Figs. 3(c) and 3(d), respectively. We find that the band gap closes when c is compressed by about 5%, and it reopens with further compression, which indicates that MnSb$_2$Te$_4$ becomes an AFM TI. For the case of 6% compressive strain, the Z_2 invariant is 1, as shown by the Wilson loop in Fig. 3(e), indicating that the band inversion occurred at Γ. We calculate the surface states of 6% compressive strain for the $(1\bar{1}0)$ surface in Fig. 3(f), which is a surface that preserves the symmetry $S = \Theta\tau_{1/2}$ [21,22]. It is clear that there is a Dirac-cone-like topological surface state in the band gap connecting the conduction and valence bands, although the band gap is so small that the Dirac cone is buried beneath the bulk states. On the contrary, we can see only a trivial gapped surface state on the (111) surface, which does not preserve S symmetry.

B. FM state of MnSb$_2$Te$_4$

The electronic structures of FM MnSb$_2$Te$_4$ calculated without and with SOC are shown in Figs. 4(a) and 4(b), respectively. There is a direct band gap of about 0.21 eV between the spin-up and spin-down bands at the Γ point without SOC. When SOC is taken into account, there is a very small gap of about 7.75 meV at the Γ point, which is different from the FM state of MnBi$_2$Te$_4$.

To check the topological quantum of FM MnSb$_2$Te$_4$, we calculate the topological index z_4 using the parity eigenvalue $p_n(\Lambda)$ of occupied states n at eight time-reversal-invariant momenta (TRIM) Λ since the inversion symmetry is kept [47,49]. z_4 is defined as

$$z_4 = \sum_{\Lambda \in TRIM} \sum_{n \in occ} \frac{1 + p_n(\Lambda)}{2} \bmod 4. \tag{1}$$

A value of $z_4 = 1, 3$ means a WSM phase, where an odd number of Weyl nodes exists in half of the BZ. The value

$z_4 = 2$ indicates an axion insulator. The above AFM TI state after tuning can also be considered an axion insulator. We find that the FM MnSb$_2$Te$_4$ with an ideal lattice structure based on experimental data is a trivial insulator with a full gap throughout the whole BZ with $z_4 = 0$. The parity eigenvalues of the bands around the Fermi level at Γ are indicated by + or − in Fig. 4(b) since only the bands at Γ will have band inversion during the tuning. In order to realize the WSM state, we pressurized the FM structure of MnSb$_2$Te$_4$ along the c axis as done in the AFM case. Figures 5(a) and 5(b) show the calculated bands of the FM structure compressed by 1% and 3%, respectively. Through the parity configuration of the bands at Γ, one can immediately find that z_4 changes from 0 to 1, indicating there is an odd number of Weyl nodes in half of the BZ. In comparison with the AFM state, 1% compression is enough to drive the topological phase transition and generates cross points, i.e., Weyl nodes. We have found that the Weyl nodes are on the Γ-Z path, i.e., on the C_{3z} rotation axis. The C_{3z} symmetry is preserved in both the AFM and FM states we studied with the Mn local magnetic moment pointing parallel to the axis. The inversion symmetry relates the Weyl node in the $k_z > 0$ BZ to its pair partner of opposite chirality in the $k_z < 0$ BZ. If the Weyl nodes are away from the C_{3z} rotation axis, there will be at least three (an odd number) pairs of them in the whole BZ. These Weyl nodes are type I with upright cones, as shown in the insets of Figs. 5(a) and 5(b). We choose the structure under 3% compressive strain to show its Weyl nodes, surface states, and Fermi arc. As shown in Fig. 5(e), we calculate the surface states on the $(1\bar{1}0)$ surface where k_z is along the projection line of path Γ-Z of the 3D BZ. The two Weyl nodes are projected close to the $\bar{\Gamma}$ point above the Fermi level. Their chiralities are 1 and −1, and the energy is very close to the Fermi level ($E_{arc} \approx 0.007$ eV). There is a very clear Fermi arc connecting the projections of the two Weyl nodes, as depicted in Fig. 5(f). These are obvious and typical characterizations of type-I WSMs [50–52]. It is known that the insulating electronic state constrained within the two-dimensional plane perpendicular to k_z will have different Chern numbers C when the plane is located between the two Weyl nodes and out of them, as indicated in Fig. 5(f) [53,54]. This distribution of C is consistent with the number of crossing points between the Fermi arc and a reference line in the horizontal direction,
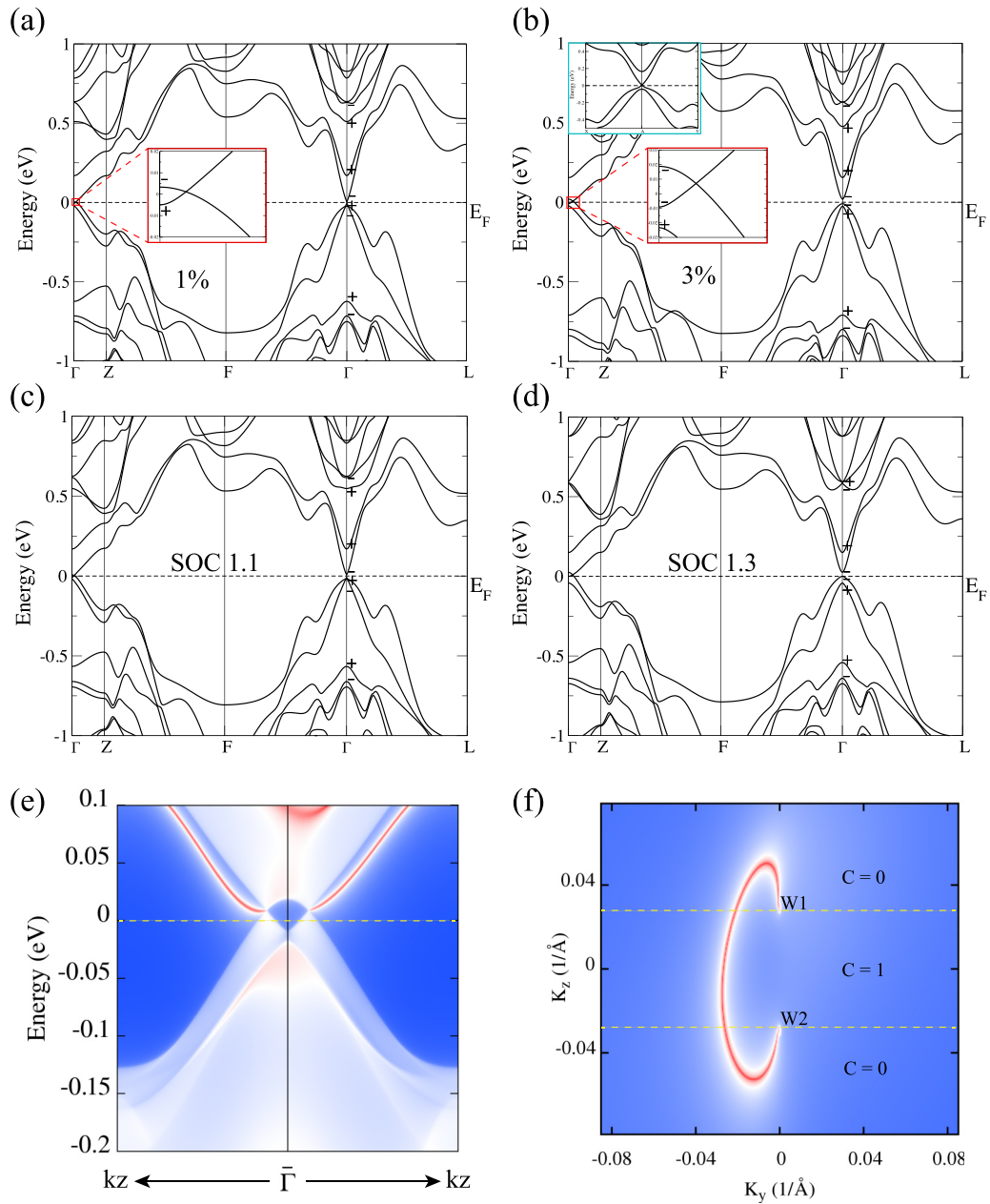
FIG. 5. The electronic structures of FM MnSb$_2$Te$_4$ under different conditions. (a) and (b) The band structures with interlayer distances decreased by 1% and 3% with SOC, respectively. [The inset with the blue border shows the bands along the k_x and k_y axes through the Weyl point in (b), which indicates a type-I Weyl point.] (c) and (d) Band structures for SOC strength λ_{Sb} of Sb change to 1.1 and 1.3 times the initial value, respectively. (e) Surface state for the case with 3% compressive strain on the $(1\bar{1}0)$ surfaces. There are two Weyl nodes along the k_z direction. (f) Fermi arc connecting the projections of Weyl nodes W1 and W2 at 0.007 eV.

namely, an even number of times (zero or two) in the region with $C = 0$ and an odd number of times (one) in the region with $C = 1$.

We also adjust the SOC strength of Sb for the FM state with 1.1 and 1.3 times the initial SOC strength λ_0, and the calculated bands are shown in Figs. 5(c) and 5(d). Compared with the AFM case, a topological phase transition for the FM state is more likely to occur, and the Weyl nodes can emerge when SOC is enhanced only 0.1 times.

In the Appendix, we check the band structure for the crystal structure determined in Ref. [30] without Sb and Mn site mixing. The calculation is performed for the FM state within GGA and without considering U. The inter-layer distance effect, as well as various van der Waals corrections, are also considered. The type-II Weyl nodes proposed in Ref. [30] have not been reproduced in these attempts.

IV. SUMMARY

We mainly investigated the electronic structures, band topology, and surface states of the AFM and FM states of the layered magnetic material MnSb$_2$Te$_4$, which has been synthesized experimentally. Although the samples showed
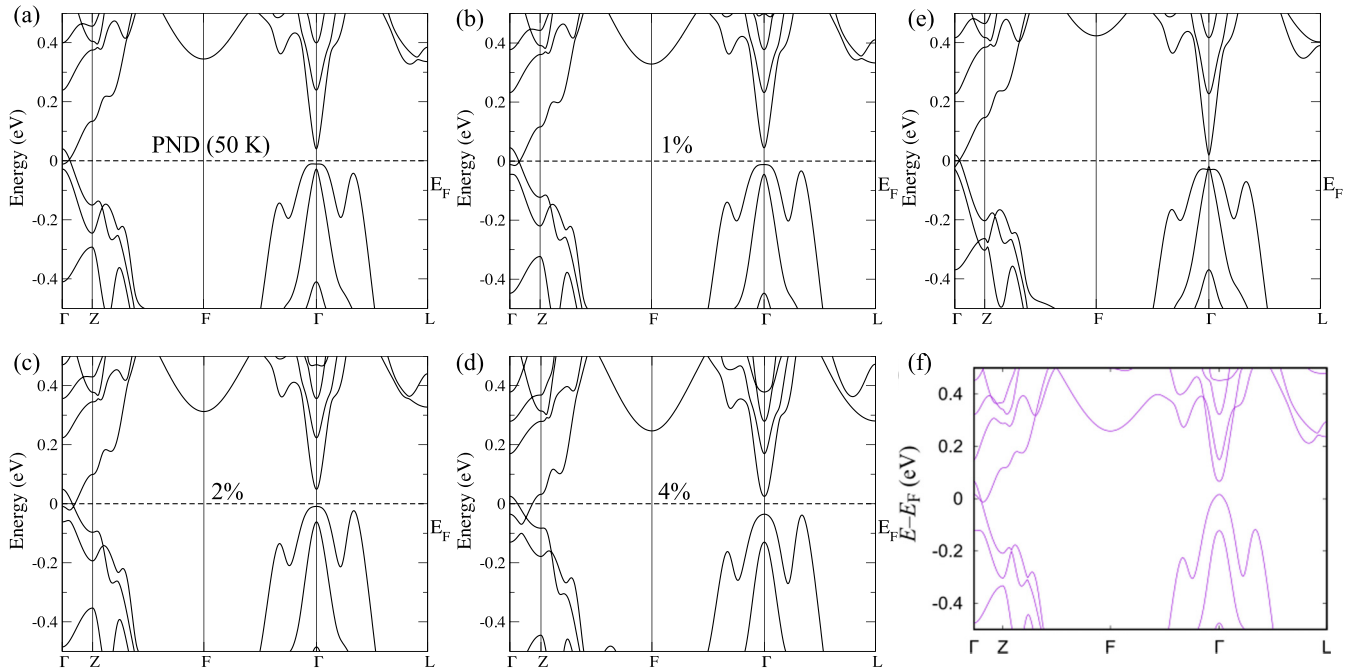
FIG. 6. The band structure of MnSb$_2$Te$_4$ for the crystal structure from Ref. [30] determined by PND at 50 K in the FM state within GGA. SOC is included. (a) The band structure without any modification of the crystal structure. (b)–(d) The band structure with interlayer distance decreased by 1%, 2%, and 4% along the z axis, respectively. (e) The band structure of MnSb$_2$Te$_4$ from the crystal structure in our work. (f) The band structure of MnSb$_2$Te$_4$ adapted from Ref. [30].

mixing of Mn and Sb sites, we used the crystal structure without site mixing to study the effects of SOC strength and uniaxial strain through first-principles calculations. We found that in the AFM state, the SOC strength of Sb is so small that MnSb$_2$Te$_4$ is not an AFM TI. However, the band inversion can be realized, and MnSb$_2$Te$_4$ becomes an AFM TI when the interlayer distance is decreased by more than 5% or the SOC strength λ_{Sb} of Sb is increased to more than 1.3 times the initial value. In the FM state, MnSb$_2$Te$_4$ is not a WSM in its ideal crystal structure. The compressive strain decreasing the interlayer distance by about 1% or increasing λ_{Sb} by 10% can cause the Weyl nodes to emerge and can lead MnSb$_2$Te$_4$ to become a type-I WSM. The Weyl nodes appear on the Γ-Z path, and they are type-I upright Weyl cones.
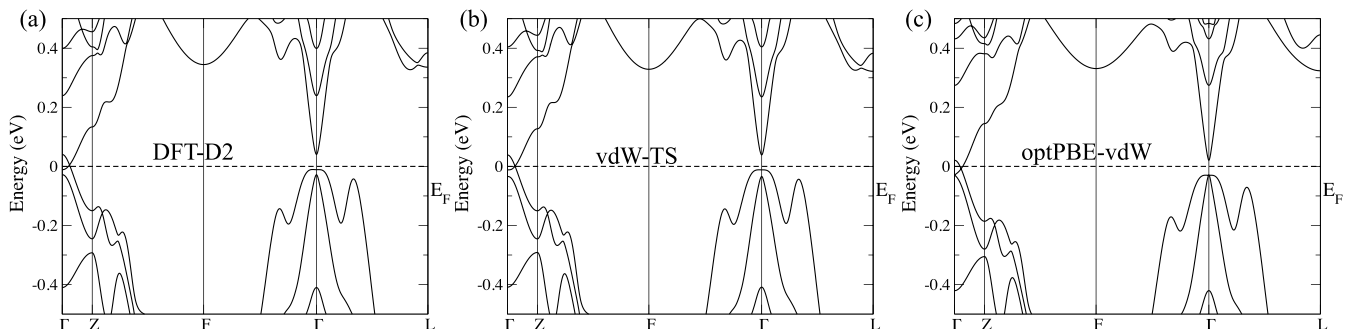
FIG. 7. The band structure of MnSb$_2$Te$_4$ calculated for the crystal structure from Ref. [30] determined by PND at 50 K in the FM state with different vdW corrections including SOC.

APPENDIX: THE BAND STRUCTURE FROM THE CRYSTAL STRUCTURE IN REFERENCE [30] WITHOUT U

In this Appendix, we construct the crystal structure of $MnSb_2Te_4$ by using the data in Table I of Ref. [30] without Sb-Mn intermixing; that is, the atomic sites are from Powder neutron-diffraction (PND) at 50 K, and the lattice constants are $a = 4.2219(2)$ Å and $c = 40.606(3)$ Å. The band structures have been calculated for the FM state within GGA and without including the Hubbard U parameter. We find the following:

(1) In Fig. 6(a), the crystal structure is taken to be that in Table I of Ref. [30]. The band structure we calculated is nearly the same as that [Fig. 6(e)] from the crystal structure in our work.

(2) We tried to tune the interlayer distance [Figs. 6(b)–6(d)] based on the crystal structure from Ref. [30]. As we can see, the band structure along Γ-Z varies as the interlayer distance changes. If we examine the bands around the Weyl node, we find that it is still type I instead of type II. The band in Ref. [30] is shown in Fig. 6(f) for comparison.

We have also tried the DFT calculation with various van der Waals (vdW) corrections using VASP. The results are shown in Fig. 7.

[1] L. Fu, C. L. Kane, and E. J. Mele, Topological Insulators in Three Dimensions, Phys. Rev. Lett. **98**, 106803 (2007).

[2] L. Fu and C. L. Kane, Topological insulators with inversion symmetry, Phys. Rev. B **76**, 045302 (2007).

[3] M. Z. Hasan and C. L. Kane, Colloquium: Topological insulators, Rev. Mod. Phys. **82**, 3045 (2010).

[4] X.-L. Qi and S.-C. Zhang, Topological insulators and superconductors, Rev. Mod. Phys. **83**, 1057 (2011).

[5] X.-L. Qi, T. L. Hughes, and S.-C. Zhang, Topological field theory of time-reversal invariant insulators, Phys. Rev. B **78**, 195424 (2008).

[6] X.-L. Qi, T. L. Hughes, and S.-C. Zhang, Fractional charge and quantized current in the quantum spin Hall state, Nat. Phys. **4**, 273 (2008).

[7] R. Li, J. Wang, X.-L. Qi, and S.-C. Zhang, Dynamical axion field in topological magnetic insulators, Nat. Phys. **6**, 284 (2010).

[8] N. Varnava and D. Vanderbilt, Surfaces of axion insulators, Phys. Rev. B **98**, 245117 (2018).

[9] C. Yue, Y. Xu, Z. Song, H. Weng, Y.-M. Lu, C. Fang, and X. Dai, Symmetry-enforced chiral hinge states and surface quantum anomalous Hall effect in the magnetic axion insulator $Bi_{2-x}Sm_xSe_3$, Nat. Phys. **15**, 577 (2019).

[10] Y. Xu, Z. Song, Z. Wang, H. Weng, and X. Dai, Higher-Order Topology of the Axion Insulator $EuIn_2As_2$, Phys. Rev. Lett. **122**, 256402 (2019).

[11] C. Liu, Y. Wang, H. Li, Y. Wu, Y. Li, J. Li, K. He, Y. Xu, J. Zhang, and Y. Wang, Robust axion insulator and Chern insulator phases in a two-dimensional antiferromagnetic topological insulator, Nat. Mater. **19**, 522 (2020).

[12] F. D. M. Haldane, Model for a Quantum Hall Effect without Landau Levels: Condensed-Matter Realization of the "Parity Anomaly," Phys. Rev. Lett. **61**, 2015 (1988).

[13] R. Yu, W. Zhang, H.-J. Zhang, S.-C. Zhang, X. Dai, and Z. Fang, Quantized anomalous Hall effect in magnetic topological insulators, Science **329**, 61 (2010).

[14] C.-X. Liu, X.-L. Qi, X. Dai, Z. Fang, and S.-C. Zhang, Quantum Anomalous Hall Effect in $Hg_{1-y}Mn_yTe$ Quantum Wells, Phys. Rev. Lett. **101**, 146802 (2008).

[15] K. Nomura and N. Nagaosa, Surface-Quantized Anomalous Hall Current and the Magnetoelectric Effect in Magnetically Disordered Topological Insulators, Phys. Rev. Lett. **106**, 166802 (2011).

[16] Y. Deng, Y. Yu, M. Z. Shi, Z. Guo, Z. Xu, J. Wang, X. H. Chen, and Y. Zhang, Quantum anomalous Hall effect in intrinsic magnetic topological insulator $MnBi_2Te_4$, Science **367**, 895 (2020).

[17] H. Zhang, C.-X. Liu, X.-L. Qi, X. Dai, Z. Fang, and S.-C. Zhang, Topological insulators in Bi_2Se_3, Bi_2Te_3 and Sb_2Te_3 with a single Dirac cone on the surface, Nat. Phys. **5**, 438 (2009).

[18] Y. Chen, J. G. Analytis, J.-H. Chu, Z. Liu, S.-K. Mo, X.-L. Qi, H. Zhang, D. Lu, X. Dai, Z. Fang *et al.*, Experimental realization of a three-dimensional topological insulator, Bi_2Te_3, Science **325**, 178 (2009).

[19] C.-Z. Chang, J. Zhang, X. Feng, J. Shen, Z. Zhang, M. Guo, K. Li, Y. Ou, P. Wei, L.-L. Wang *et al.*, Experimental observation of the quantum anomalous Hall effect in a magnetic topological insulator, Science **340**, 167 (2013).

[20] C.-Z. Chang, W. Zhao, D. Y. Kim, H. Zhang, B. A. Assaf, D. Heiman, S.-C. Zhang, C. Liu, M. H. Chan, and J. S. Moodera, High-precision realization of robust quantum anomalous Hall state in a hard ferromagnetic topological insulator, Nat. Mater. **14**, 473 (2015).

[21] J. Li, Y. Li, S. Du, Z. Wang, B.-L. Gu, S.-C. Zhang, K. He, W. Duan, and Y. Xu, Intrinsic magnetic topological insulators in van der Waals layered $MnBi_2Te_4$-family materials, Sci. Adv. **5**, eaaw5685 (2019).

[22] D. Zhang, M. Shi, T. Zhu, D. Xing, H. Zhang, and J. Wang, Topological Axion States in the Magnetic Insulator $MnBi_2Te_4$ with the Quantized Magnetoelectric Effect, Phys. Rev. Lett. **122**, 206401 (2019).

[23] M. Otrokov, I. Klimovskikh, H. Bentmann, D. Estyunin, A. Zeugner, Z. Aliev, S. Gaß, A. Wolter, A. Koroleva, A. Shikin *et al.*, Prediction and observation of an antiferromagnetic topological insulator, Nature (London) **576**, 416 (2019).

[24] S. Chowdhury, K. F. Garrity, and F. Tavazza, Prediction of Weyl semimetal and antiferromagnetic topological insulator phases in Bi_2MnSe_4, npj Comput. Mater. **5**, 33 (2019).

[25] R.-X. Zhang, F. Wu, and S. Das Sarma, Möbius Insulator and Higher-Order Topology in $MnBi_{2n}Te_{3n+1}$, Phys. Rev. Lett. **124**, 136407 (2020).

[26] S. Eremeev, M. Otrokov, and E. V. Chulkov, Competing rhombohedral and monoclinic crystal structures in $MnPn_2Ch_4$ compounds: An *ab-initio* study, J. Alloys Compd. **709**, 172 (2017).

[27] M. M. Otrokov, I. P. Rusinov, M. Blanco-Rey, M. Hoffmann, A. Y. Vyazovskaya, S. V. Eremeev, A. Ernst, P. M. Echenique,

A. Arnau, and E. V. Chulkov, Unique Thickness-Dependent Properties of the van der Waals Interlayer Antiferromagnet MnBi$_2$Te$_4$ Films, Phys. Rev. Lett. **122**, 107202 (2019).

[28] J.-Q. Yan, S. Okamoto, M. A. McGuire, A. F. May, R. J. McQueeney, and B. C. Sales, Evolution of structural, magnetic, and transport properties in MnBi$_{2-x}$Sb$_x$Te$_4$, Phys. Rev. B **100**, 104409 (2019).

[29] P. Swatek, Y. Wu, L.-L. Wang, K. Lee, B. Schrunk, J. Yan, and A. Kaminski, Gapless Dirac surface states in the antiferromagnetic topological insulator MnBi$_2$Te$_4$, Phys. Rev. B **101**, 161109(R) (2020).

[30] T. Murakami, Y. Nambu, T. Koretsune, G. Xiangyu, T. Yamamoto, C. M. Brown, and H. Kageyama, Realization of interlayer ferromagnetic interaction in MnSb$_2$Te$_4$ toward the magnetic Weyl semimetal state, Phys. Rev. B **100**, 195103 (2019).

[31] Y. Li, Z. Jiang, J. Li, S. Xu, and W. Duan, Magnetic anisotropy of the two-dimensional ferromagnetic insulator MnBi$_2$Te$_4$, Phys. Rev. B **100**, 134438 (2019).

[32] H. Li, S.-Y. Gao, S.-F. Duan, Y.-F. Xu, K.-J. Zhu, S.-J. Tian, J.-C. Gao, W.-H. Fan, Z.-C. Rao, J.-R. Huang, J.-J. Li, D.-Y. Yan, Z.-T. Liu, W.-L. Liu, Y.-B. Huang, Y.-L. Li, Y. Liu, G.-B. Zhang, P. Zhang, T. Kondo, S. Shin, H.-C. Lei, Y.-G. Shi, W.-T. Zhang, H.-M. Weng, T. Qian, and H. Ding, Dirac Surface States in Intrinsic Magnetic Topological Insulators EuSn$_2$As$_2$ and MnBi$_{2n}$Te$_{3n+1}$, Phys. Rev. X **9**, 041039 (2019).

[33] J.-Q. Yan, Q. Zhang, T. Heitmann, Z. Huang, K. Y. Chen, J.-G. Cheng, W. Wu, D. Vaknin, B. C. Sales, and R. J. McQueeney, Crystal growth and magnetic structure of MnBi$_2$Te$_4$, Phys. Rev. Mater. **3**, 064202 (2019).

[34] B. Chen, F. Fei, D. Zhang, B. Zhang, W. Liu, S. Zhang, P. Wang, B. Wei, Y. Zhang, Z. Zuo *et al.*, Intrinsic magnetic topological insulator phases in the Sb doped MnBi$_2$Te$_4$ bulks and thin flakes, Nat. Commun. **10**, 1 (2019).

[35] J. Ge, Y. Liu, J. Li, H. Li, T. Luo, Y. Wu, Y. Xu, and J. Wang, High-Chern-Number and High-Temperature Quantum Hall Effect without Landau Levels, Natl. Sci. Rev. (2020), doi: 10.1093/nsr/nwaa089.

[36] D. S. Lee, T.-H. Kim, C.-H. Park, C.-Y. Chung, Y. S. Lim, W.-S. Seo, and H.-H. Park, Crystal structure, properties and nanostructuring of a new layered chalcogenide semiconductor, Bi$_2$MnTe$_4$, CrystEngComm **15**, 5532 (2013).

[37] S. H. Lee, Y. Zhu, H. Yi, D. Graf, R. Basnet, A. Fereidouni, A. Wegner, Y.-F. Zhao, L. Min, K. Verlinde *et al.*, Transport evidence for a magnetic-field induced ideal Weyl state in antiferromagnetic topological insulator MnBi$_2$Te$_4$, arXiv:2002.10683.

[38] G. Shi, M. Zhang, D. Yan, H. Feng, M. Yang, Y. Shi, and Y. Li, Anomalous Hall Effect in Layered Ferrimagnet MnSb$_2$Te$_4$, Chin. Phys. Lett. **37**, 047301 (2020).

[39] G. Kresse and J. Furthmüller, Efficient iterative schemes for *ab initio* total-energy calculations using a plane-wave basis set, Phys. Rev. B **54**, 11169 (1996).

[40] G. Kresse and D. Joubert, From ultrasoft pseudopotentials to the projector augmented-wave method, Phys. Rev. B **59**, 1758 (1999).

[41] J. P. Perdew, K. Burke, and M. Ernzerhof, Generalized Gradient Approximation Made Simple, Phys. Rev. Lett. **77**, 3865 (1996).

[42] M. Cococcioni and S. de Gironcoli, Linear response approach to the calculation of the effective interaction parameters in the LDA + U method, Phys. Rev. B **71**, 035105 (2005).

[43] H. J. Kulik, M. Cococcioni, D. A. Scherlis, and N. Marzari, Density Functional Theory in Transition-Metal Chemistry: A Self-Consistent Hubbard *U* Approach, Phys. Rev. Lett. **97**, 103001 (2006).

[44] Q. Wu, S. Zhang, H.-F. Song, M. Troyer, and A. A. Soluyanov, WannierTools: An open-source software package for novel topological materials, Comput. Phys. Commun. **224**, 405 (2018).

[45] A. A. Mostofi, J. R. Yates, Y.-S. Lee, I. Souza, D. Vanderbilt, and N. Marzari, wannier90: A tool for obtaining maximally-localised Wannier functions, Comput. Phys. Commun. **178**, 685 (2008).

[46] R. S. K. Mong, A. M. Essin, and J. E. Moore, Antiferromagnetic topological insulators, Phys. Rev. B **81**, 245209 (2010).

[47] A. M. Turner, Y. Zhang, R. S. K. Mong, and A. Vishwanath, Quantized response and topology of magnetic insulators with inversion symmetry, Phys. Rev. B **85**, 165120 (2012).

[48] R. Yu, X. L. Qi, A. Bernevig, Z. Fang, and X. Dai, Equivalent expression of $\mathbb{Z}_2$ topological invariant for band insulators using the non-Abelian Berry connection, Phys. Rev. B **84**, 075119 (2011).

[49] Y. Xu, L. Elcoro, Z. Song, B. J. Wieder, M. G. Vergniory, N. Regnault, Y. Chen, C. Felser, and B. A. Bernevig, High-throughput calculations of antiferromagnetic topological materials from magnetic topological quantum chemistry, arXiv:2003.00012.

[50] H. Weng, C. Fang, Z. Fang, B. A. Bernevig, and X. Dai, Weyl Semimetal Phase in Noncentrosymmetric Transition-Metal Monophosphides, Phys. Rev. X **5**, 011029 (2015).

[51] S.-Y. Xu, I. Belopolski, N. Alidoust, M. Neupane, G. Bian, C. Zhang, R. Sankar, G. Chang, Z. Yuan, C.-C. Lee *et al.*, Discovery of a Weyl fermion semimetal and topological Fermi arcs, Science **349**, 613 (2015).

[52] B. Q. Lv, H. M. Weng, B. B. Fu, X. P. Wang, H. Miao, J. Ma, P. Richard, X. C. Huang, L. X. Zhao, G. F. Chen, Z. Fang, X. Dai, T. Qian, and H. Ding, Experimental Discovery of Weyl Semimetal TaAs, Phys. Rev. X **5**, 031013 (2015).

[53] G. Xu, H. Weng, Z. Wang, X. Dai, and Z. Fang, Chern Semimetal and the Quantized Anomalous Hall Effect in HgCr$_2$Se$_4$, Phys. Rev. Lett. **107**, 186806 (2011).

[54] H. Weng, R. Yu, X. Hu, X. Dai, and Z. Fang, Quantum anomalous Hall effect and related topological electronic states, Adv. Phys. **64**, 227 (2015).